JACS
JOURNAL OF THE AMERICAN CHEMICAL SOCIETY
pubs.acs.org/JACS
Article

Stabilizing Highly Active Ru Sites by Suppressing Lattice Oxygen Participation in Acidic Water Oxidation

Yunzhou Wen,[○] Peining Chen,[○] Lu Wang,[○] Shangyu Li,[○] Ziyun Wang, Jehad Abed, Xinnan Mao, Yimeng Min, Cao Thang Dinh, Phil De Luna, Rui Huang, Longsheng Zhang, Lie Wang, Liping Wang, Robert J. Nielsen, Huihui Li, Taotao Zhuang, Changchun Ke, Oleksandr Voznyy, Yongfeng Hu, Youyong Li, William A. Goddard III, Bo Zhang,* Huisheng Peng,* and Edward H. Sargent*

Cite This: *J. Am. Chem. Soc.* 2021, 143, 6482−6490

ABSTRACT: In hydrogen production, the anodic oxygen evolution reaction (OER) limits the energy conversion efficiency and also impacts stability in proton-exchange membrane water electrolyzers. Widely used Ir-based catalysts suffer from insufficient activity, while more active Ru-based catalysts tend to dissolve under OER conditions. This has been associated with the participation of lattice oxygen (lattice oxygen oxidation mechanism (LOM)), which may lead to the collapse of the crystal structure and accelerate the leaching of active Ru species, leading to low operating stability. Here we develop Sr−Ru−Ir ternary oxide electrocatalysts that achieve high OER activity and stability in acidic electrolyte. The catalysts achieve an overpotential of 190 mV at 10 mA cm^{-2} and the overpotential remains below 225 mV following 1,500 h of operation. X-ray absorption spectroscopy and ^{18}O isotope-labeled online mass spectroscopy studies reveal that the participation of lattice oxygen during OER was suppressed by interactions in the Ru−O−Ir local structure, offering a picture of how stability was improved. The electronic structure of active Ru sites was modulated by Sr and Ir, optimizing the binding energetics of OER oxo-intermediates.

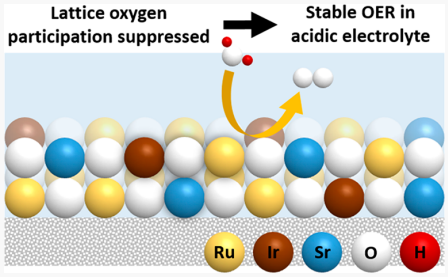

INTRODUCTION

Proton-exchange membrane (PEM) water electrolysis is a promising technology for hydrogen production thanks to its high current density, rapid system response, and low gas crossover rate.[1−3] The energy conversion efficiency and durability of a PEM electrolyzer are mainly determined by the anodic oxygen evolution reaction (OER), which involves a sluggish four-electron transfer kinetic process. The harsh acidic and oxidative environment of the PEM limits the practical application of most OER electrocatalysts. Only iridium (Ir) and Ir-based oxides possess adequate corrosion resistance.[2,4,5] Unfortunately, due to the scarcity and relatively low OER activity of Ir, such catalysts do not meet the demands of PEM electrolyzers at scale.[1,2] Developing stable, highly active, and cost-effective OER catalysts under acidic conditions is a challenge yet to be overcome.

Understanding the mechanism of OER can effectively guide the rational design of high-performance electrocatalysts. In the conventional adsorption evolution mechanism (AEM), the OER activity is affected by the adsorption energetics of oxo-intermediates, and the optimization of these is limited by the scaling relationship.[6,7] In recent years, a new lattice oxygen oxidation mechanism (LOM) was discovered, involving direct O−O coupling between the oxo-intermediates and lattice oxygen,[8−10] and has been widely studied in both alkaline and neutral conditions as it usually exhibits faster OER kinetics than the conventional AEM pathway.[11−13]

It has been shown that, in acidic conditions, Ru-based electrocatalysts suffer from the participation of lattice oxygen and that this contributes to the collapse of the crystal structure and accelerates the leaching of active Ru species at defective domains.[8,9,14] The soluble high-valence intermediates and LOM pathway increase OER kinetics in Ru-based catalysts, but such high activity is lost after a few hours.[15−17] Under acidic conditions, increasing the OER activity at the expense of stability using the LOM pathway is an approach that requires further work.

LOM has been rarely observed for rutile IrO_2 during OER,[8,9,18] a result of the stronger Ir−O bonding in rutile structures than in perovskites[9,19] and pyrochlores.[20,21] We took the view that integrating Ir into rutile RuO_2 could offer a route to suppress the participation of lattice oxygen in the OER, thereby enhancing stability. However, this will concurrently

Received: January 12, 2021
Published: April 23, 2021

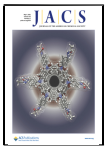

https://doi.org/10.1021/jacs.1c00384
J. Am. Chem. Soc. 2021, 143, 6482−6490

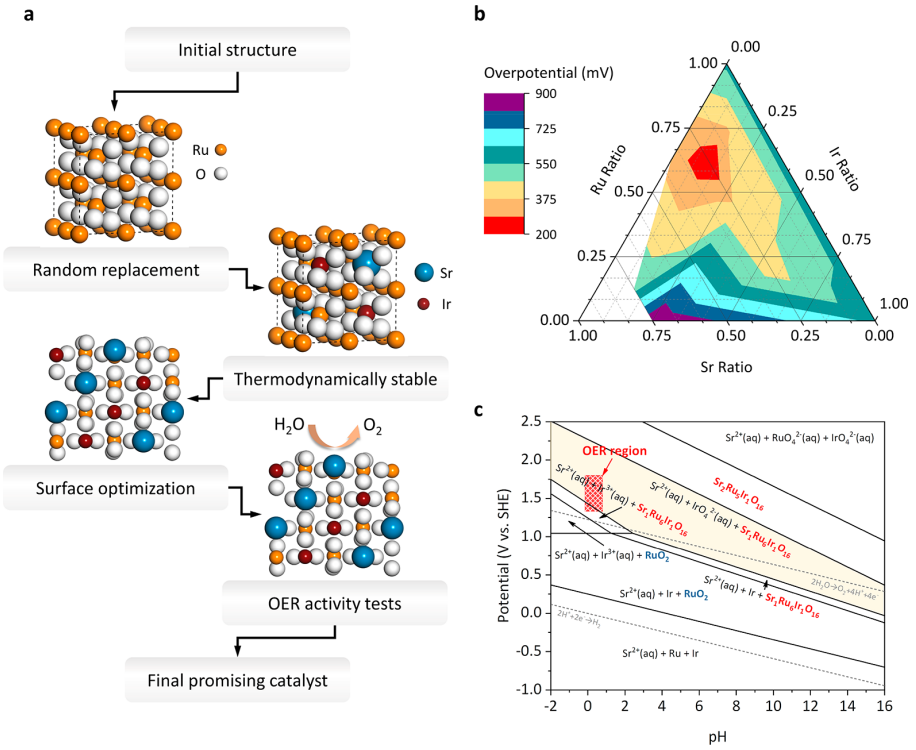

Figure 1. High-throughput screening of electrocatalysts for OER. (a) DFT workflow of high-throughput screening. (b) Calculated OER overpotential with different ternary compositions. The three edges of the ternary plot correspond to the ratio of two metal elements (i.e., Ir−Sr, Ir−Ru, and Sr−Ru). The red region represents the Sr−Ru−Ir ratios with lowest OER overpotential. (c) Pourbaix diagram of $Sr_2Ru_5Ir_1O_{16}$ and $Sr_1Ru_6Ir_1O_{16}$ oxide calculated using DFT: the $Sr_1Ru_6Ir_1O_{16}$ phase is stable in the OER region.

reduce the activity of Ru because the flexibility of Ru redox is limited by Ir dopants.[14,22−26] To date, strategies to simultaneously achieve activity and stability are still elusive.

Here we pursued a dual-modulation strategy to suppress the LOM and tune the electronic structures of active Ru sites. We incorporated small amounts of alkali-earth metal (Sr) and Ir into the rutile Ru-based oxide. Using density functional theory (DFT) screening, we optimized the ratio of the two modulators (Sr, Ir) to obtain the high active and stable Ru sites. We then synthesized these catalysts by a sol−gel method. The best-performing SrRuIr oxide catalyst achieved low overpotential of 190 mV at 10 mA cm^{-2} and the overpotential was maintained at 223 mV following 1,500 operating hours. The improved stability was found to originate from interactions within the Ru−O−Ir local structure, suppressing the LOM pathway during OER. The high activity was a result of optimized oxo-intermediate binding energetics on the high-valence Ru sites formed after Sr and Ir incorporation. When applied in a PEM electrolyzer, the new catalyst achieved a low full cell voltage of 1.50 V at 1 A cm^{-2}.

RESULTS AND DISCUSSION

DFT Screening of Optimal Sr−Ru−Ir Ternary Electrocatalysts for OER. We first screened for optimal ternary Sr−Ru−Ir oxide electrocatalysts via high-throughput DFT calculations. We started from the pure rutile RuO_2 structures. By randomly replacing the Ru atoms with Sr or Ir, we chose the ten most thermodynamically stable ternary oxide crystals with different ratios from 2,201 different structures (Figure 1a and Figure S1). The DFT calculations suggest that the incorporation of Sr and Ir will expand the rutile lattice and increase the degree of disorder of crystals (Figure S2). We then calculated the OER overpotential from the adsorption free energies of OER intermediates (OH*, O*, and OOH*) on the (110) surface of selected models, since (110) is regarded as the most stable surface of RuO_2.[6,27] In all cases, the OER intermediates prefer to adsorb on the Ru sites rather than the Ir or Sr sites, a finding suggestive that Ru is the active site. The calculated OER overpotentials of catalysts with different Sr−Ru−Ir ratios (Figure 1b and Table S1−2) are presented in a ternary composition diagram with the molar ratios among the constituent elements on the vertices. The lowest calculated overpotential was ∼210 mV located in the red region in Figure 1b. In this region, the ratios of different elements are approximately 0.15−0.25 for Sr, 0.6−0.7 for Ru, and 0.05−0.2 for Ir, respectively. Toward the active catalysts, we further evaluated the stability in aqueous solution by calculating the Pourbaix diagram. Figure 1c depicts phase stability in Pourbaix diagrams for the most OER active $Sr_2Ru_5Ir_1O_{16}$ phases in an aqueous environment with respect to the dissolved and solid phases (Table S3). Under the working potential (U = 1.4 to 2 V vs standard hydrogen electrode (SHE)) and electrolyte pH range (pH = 0 to 1) of acidic OER, a portion of Sr and Ir will leach out to form a stable $Sr_1Ru_6Ir_1O_{16}$ phase. This phase has the potential to be both active and stable toward OER.

Material Synthesis and Electrochemical Performances. In light of DFT predictions, we synthesized Sr−Ru−Ir ternary catalysts with different compositions. A sol−gel

https://doi.org/10.1021/jacs.1c00384
J. Am. Chem. Soc. 2021, 143, 6482−6490

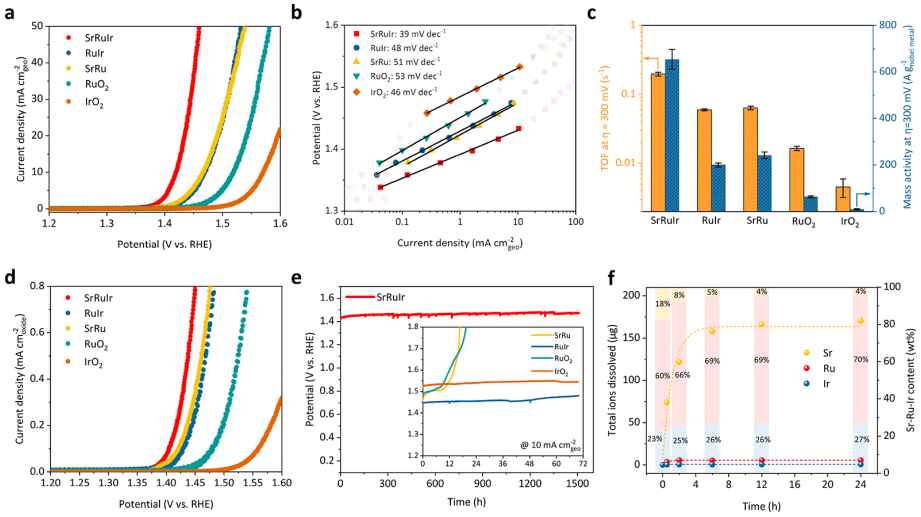

Figure 2. Electrochemical performance in a three-electrode configuration. (a) LSV curves of the best-performed SrRuIr oxide catalyst, ternary, and binary controls. (b) Tafel plots for different catalysts. (c) The TOF and mass activities of different samples. The TOF and mass activities were calculated according to total noble metal loadings. (d) LSV curves normalized by BET surface area of different catalysts to indicate intrinsic performance. (e) Chronopotentiometry stability test of SrRuIr and control samples at 10 mA cm^{-2}. (f) Time-dependent ion dissolution of SrRuIr oxide during OER. The scatter plot represents the actual amount of dissolved ions. The histogram represents the ion ratio that remained in the catalysts. Specifically, the catalyst film presented in the figure contains 210 μg of Sr, 0.711 μg of Ru, and 0.270 μg Ir before OER.

method followed with annealing was used to synthesize these ternary catalysts, as well as the binary and unary controls[28] (see Experimental section in the Supporting Information). X-ray diffraction (XRD) patterns showed that the as-prepared catalysts possess a rutile-type structure with low crystallinity. As seen in DFT, the incorporation of Sr and Ir led to negative shifts of the diffraction peaks (Figure S3). High-resolution transmission electron microscopy (HR-TEM) and scanning transmission electron microscopy (STEM) demonstrate that the ternary catalysts were ~4 nm rod-like nanoparticles. The elements were uniformly distributed in the catalysts to the extent that can be resolved using energy-dispersive X-ray spectroscopy (EDX) (Figure S4). These catalysts were then deposited onto glassy carbon electrodes (GCEs), and linear sweep voltammetry (LSV) was carried out in 0.5 M H_2SO_4 (pH = 0.3) to evaluate their OER performance (Figure 2a). The composition of the best-performing ternary catalyst was identified as $Sr_{1.7}Ru_5Ir_1O_{13.7}$ by EDX mapping (Table S4, denoted SrRuIr in the following text), which is close to the DFT predicted most active $Sr_2Ru_5Ir_1O_{16}$ phase. This SrRuIr oxide catalyst achieved a low overpotential of 190 ± 2 mV at 10 mA cm^{-2}_{geo}, which is ~95 mV and ~150 mV lower than that of commercial RuO_2 and IrO_2 benchmarks, respectively (Figure 2a). Binary RuIr oxide ($Ru_5Ir_{0.9}O_{11.8}$) and SrRu oxide ($Sr_{1.6}Ru_5O_{11.6}$) (denoted RuIr and SrRu, respectively) samples were synthesized under the analogous procedure. The RuIr oxides were rutile nanocrystals, while the SrRu oxides contained both the rutile and the perovskite phase (Figures S5 and S6). SrRuIr also outperformed these binary controls RuIr (239 ± 1 mV) and SrRu (238 ± 1 mV). The SrRuIr oxide catalyst exhibited a Tafel slope of 39 mV dec^{-1}, lower than that of the binary catalysts and commercial controls, indicating faster kinetics toward OER (Figure 2b). The above results indicated potential synergetic effects among Sr, Ru, and Ir.

To compare the intrinsic catalytic activities of these catalysts, we calculated their mass specific activities according to the total loading mass of noble metal and the turnover frequency (TOF) at each noble metal site (Figure 2c and Supplementary Note 1 in the Supporting Information). The SrRuIr oxide reached the highest mass specific activity of 654 A $g_{noble\ metal}^{-1}$ at η = 300 mV, which was much higher than that of SrRu (242 A g_{Ru}^{-1}), RuIr (200 A $g_{noble\ metal}^{-1}$), RuO_2 (63 A g_{Ru}^{-1}), or IrO_2 (9 A g_{Ir}^{-1}). The TOF of SrRuIr (0.20 s^{-1} at η = 300 mV) was nearly 12 and 40 times higher than that of RuO_2 (0.016 s^{-1}) and IrO_2 (0.005 s^{-1}), respectively (Table S5). To eliminate the effect of particle size and surface area, the Brunauer–Emmett–Teller (BET)-normalized surface area was adopted to compare OER currents among different catalysts (Table S6). These showed the same activity trend with TOF and mass specific activity (Figure 2d and Table S5). The electrochemical surface area (ECSA) of these catalysts was estimated by measuring double-layer capacitance in the non-Faradaic region (Figure S10 and S11). The SrRuIr oxide catalyst possessed both the highest ECSA and specific activity (Figure S12). In sum, the SrRuIr oxide catalyst possessed the highest intrinsic activity compared to controls.

We then investigated the stability of the catalysts using chronopotentiometry at a constant current density of 10 mA cm^{-2}_{geo}. The overpotential of SrRuIr at 10 mA cm^{-2}_{geo} increased from 180 mV to 210 mV in a 30 h test, to 216 mV in a 1,000 h test, and 223 mV in a 1,500 h test (Figure 2e and Figure S15). The average increase in overpotential was 0.01 mV h^{-1}; this is over 20 times slower than that of the commercial IrO_2 catalyst (0.21 mV h^{-1}). By comparison, the OER activity of RuO_2 decreased dramatically: the rate of increase in overpotential reached 5.8 mV h^{-1}, in agreement with previous reports.[14,29] The overpotential of the SrRuIr oxide catalyst after 1,500 h of continuous operation (223 mV) is 147 mV lower than the best reported RuMn oxide catalyst,[15] for which the overpotential increased from 158 mV to 370 mV after 10 h of operation (Table S7).

https://doi.org/10.1021/jacs.1c00384
J. Am. Chem. Soc. 2021, 143, 6482–6490

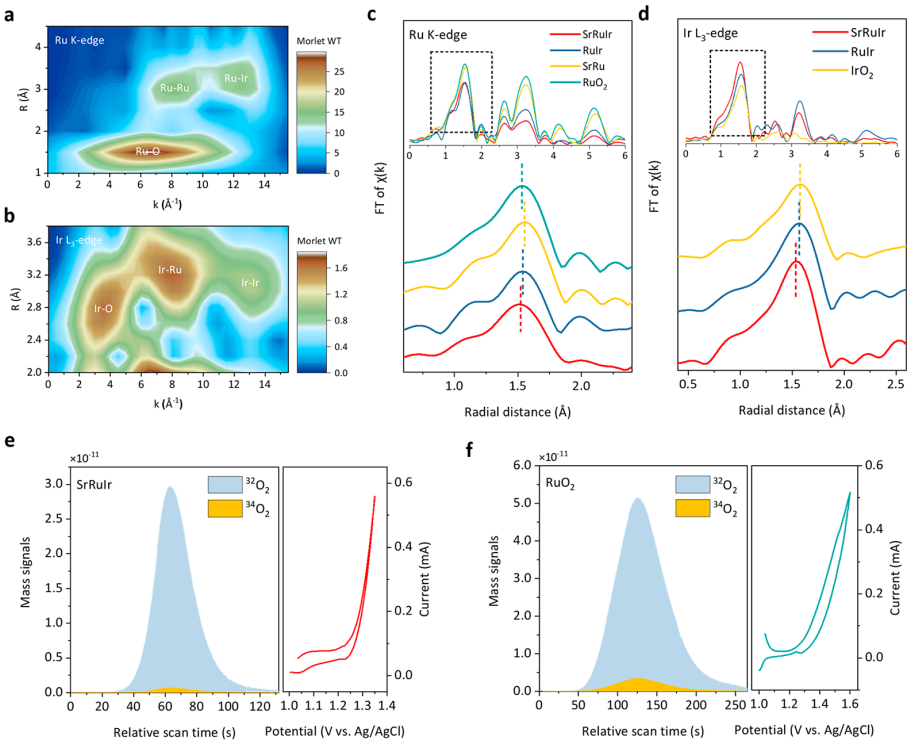

Figure 3. Structure characterization and OER mechanism analysis of SrRuIr oxide electrocatalyst. (a–b) Ru K-edge and Ir L_3-edge WT-EXAFS spectra of SrRuIr. The Morlet wavelet is used as a mother wavelet. The Morlet function parameter of $\eta = 6.5$ and $\sigma = 1$ for Ru K-edge and $\eta = 7.4$ and $\sigma = 1$ for Ir L_3-edge. (c–d) Ru K-edge FT-EXAFS spectra (k weight = 3) and Ir L_3-edge FT-EXAFS spectra (k weight = 2) of different samples, respectively. (e–f) DEMS signals of $^{32}O_2$ ($^{16}O^{16}O$) and $^{34}O_2$ ($^{16}O^{18}O$) from the reaction products for ^{18}O-labeled SrRuIr and RuO_2 catalysts in $H_2{}^{18}O$ aqueous sulfuric acid electrolyte and corresponding CV cycles. The mass spectroscopy signals are baseline subtracted.

To monitor the stability of catalysts under OER conditions, we measured ion dissolution in the electrolyte during electrolysis via inductively coupled plasma optical emission spectrometry (ICP-OES).[5,30] Figure 2f shows that Sr ions leached out of the SrRuIr catalyst rapidly at the beginning of the reaction, stabilizing after ~12 h. Ru ions experienced a slight dissolution at the very beginning of the reaction, while Ir ions were almost unchanged. With the dissolution of Sr, the overpotential was found to increase accordingly (Supplementary Note 3 in the Supporting Information). Compared with the initial state, the Sr:Ru:Ir ratio was 0.33:5:1 after Sr leaching according to the ICP-OES results. In the case of SrRu, severe leaching of both Sr and Ru from the structure was accompanied by a dramatic loss in activity (Figure 2e and Figure S16). On the basis of the ICP-OES data, we estimated the stability number (S-number) of the catalysts.[9] The S-number for SrRuIr is approximately 2 orders of magnitude higher than SrRu (Table S8), consistent with a role for the Ir dopant in stabilizing the catalyst.

We then investigated the structure and composition of SrRuIr catalyst after OER. A slight increase in the size of some particles was observed (Figure S17a–c). This may be due to the increasing structural order of catalysts along with the Sr leaching. Fast Fourier transformation (FFT) and inverse FFT of the select area in Figure S17d indicated that the SrRuIr remained as a rutile structure after OER, while the *d*-spacing was 3.38 and 2.82 Å for (110) and (101) plane, respectively. These values were larger than the pristine RuO_2 (3.18 and 2.56 Å), which can be ascribed to heteroatom incorporation. The EDX elemental mapping indicated that part of Sr was retained in the lattice of the SrRuIr catalyst after OER (Figure S17g–k), and the Sr:Ru:Ir ratio was 0.36:5:1.14, consistent with ICP-OES results. The composition of the near-edge region after OER was examined by X-ray photoelectron microscopy (XPS) (Figure S29–30, Figure S35, and Table S12). The Sr:Ru:Ir ratio was 0.44:5:1.95 after 12 h OER and 0.38:5:1.60 after 24 h. The ICP-OES, STEM-EDX, and XPS verified the partial leaching of Sr after OER.

Local Structure of SrRuIr and the Origin of Stability. To understand the origin of the high activity and stability of SrRuIr, we investigated the local chemical environment using extended X-ray absorption fine structure (EXAFS) after OER. Ru–O–Ir local structure was observed using the wavelet transform of EXAFS (WT-EXAFS).[31] Ru–Ir scattering signals appeared in both Ru K-edge and Ir L_3-edge WT-EXAFS, indicating a strong interaction between Ru and Ir in SrRuIr (Figure 3a,b, Figure S18, and Supplementary Note 2 in the Supporting Information). Fourier-transformed EXAFS (FT-EXAFS) spectra of Ru K-edge and Ir L_3-edge revealed that the bond length of Ru–O in SrRuIr was slightly increased compared to RuO_2, while the Ir–O bonds were reduced compared to IrO_2. This indicated the interaction among Ru, O, and Ir (Figure 3c,d, Figure S20, and Table S9). It has been reported that a weak bonding of lattice oxygen may enable direct participation in the OER, forming metastable and activated complexes that are more prone to dissolution.[9]

https://doi.org/10.1021/jacs.1c00384
J. Am. Chem. Soc. 2021, 143, 6482–6490

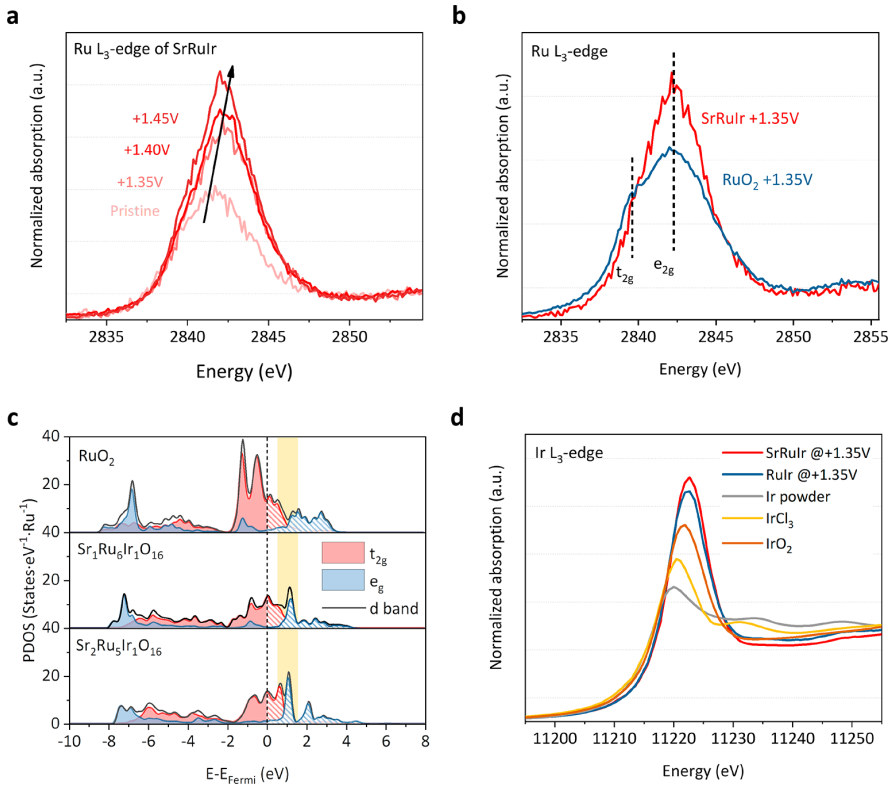

Figure 4. Electronic structure investigation of SrRuIr. (a) In situ Ru L_3-edge XAS spectra of SrRuIr: the positive peak shift indicated the increase of valence and the increasing white-line with potential indicated the unoccupied states in the e_g orbital. (b) t_{2g} and e_g band occupancy of SrRuIr and RuO_2 at the same applied potential. (c) PDOS of the Ru active site on the RuO_2, $Sr_1Ru_6Ir_1O_{16}$, and $Sr_2Ru_5Ir_1O_{16}$ surfaces calculated by DFT: Sr doping induced more unoccupied e_g states at ~1 eV above the Fermi level. (d) In situ Ir L_3-edge XAS spectra.

Therefore, the strong interaction in these Ru−O−Ir local structures may suppress the lattice oxygen involvement during OER (LOM pathway), thus improving the stability of the electrocatalyst. Such structural stability was verified by the EXAFS spectra after 120 h of electrolysis (Figure S21).

We further conducted in situ differential electrochemical mass spectroscopy (DEMS) measurements using the isotope ^{18}O to investigate the participation of lattice oxygen atoms in OER. We labeled the catalyst surface with ^{18}O and measured the evolved O_2 during OER (see Methods, Figure S22−24). The amount of $^{34}O_2$ evolved reflected the participation of lattice oxygen[11] ($^{34}O_2$ came from the combination of ^{18}O in the lattice and ^{16}O in the water). The ratio of $^{34}O_2$ generated on SrRuIr (Figure 3e) is much lower than that on RuO_2 (Figure 3f). The content of lattice oxygen participation can be quantified by performing OER cycles directly in the ^{18}O electrolyte (Figure S23). In accordance with Figure S23 and Table S10, the LOM pathway is suppressed by ~50% on SrRuIr compared to RuO_2. The majority of the evolved O_2 was generated through the AEM. The ratio of adsorbed OH and lattice O obtained in 1s measured by XPS was reduced by ~60% in SrRuIr compared to RuO_2, also indicating that less surface oxygen was involved in LOM in SrRuIr (Figure S25 and Table S11).

We then carried out *in situ* Raman spectroscopy in both ^{16}O and ^{18}O electrolyte (Figure S26). For RuO_2, three major bands at 523, 642, and 710 cm^{-1} were observed, and these we assign to E_{1g}, A_{1g}, and B_{2g} vibration modes, respectively.[32] For SrRuIr, only a broad peak at 528 cm^{-1} is observed, similar to what is seen in amorphous hydrated ruthenium oxide. When comparing the Raman spectra measured in $H_2{}^{16}O$ and $H_2{}^{18}O$ electrolyte at the 0.6 and 1.4 V (Ru^{3+}/Ru^{4+} redox potential and OER onset potential, respectively), we witness a *ca.* 5 cm^{-1} negative shift in RuO_2, while no obvious change is seen in SrRuIr (Figure S27). We associate the three bands at 523, 642, and 710 cm^{-1} in RuO_2 with Ru−O stretch vibrations.[33] Replacing lattice Ru−^{16}O with Ru−^{18}O will lead to a change in frequencies of vibration modes. The peak shift in RuO_2 may be due to the exchange of lattice oxygen with the oxygen in ^{18}O electrolyte under applied potential, while no isotope effect is observed in SrRuIr. DFT calculations also showed that the overpotential of the LOM pathway is much higher than the AEM pathway on ternary catalysts[8] (Figure S28). While with the decrease of Sr, the overpotential of LOM increased accordingly, which coincides with our experiment that the catalyst is getting stable after Sr leaching. The above results can serve as side evidence on the suppression of LOM in the SrRuIr catalyst.

Electronic Structures of Ru and Their Effects on the Improvement of OER Activity. To further understand the origin of the high activity of SrRuIr, we combined in situ X-ray absorption spectroscopy (XAS) with further DFT analysis to study the electronic structures of these electrocatalysts. With increased applied potential, the Ru L_3-edge peak at ~2840 eV shifts to higher energy, suggesting an increase in the oxidation state of Ru in SrRuIr (Figure 4a).[34] A similar valence increase

https://doi.org/10.1021/jacs.1c00384
J. Am. Chem. Soc. 2021, 143, 6482−6490

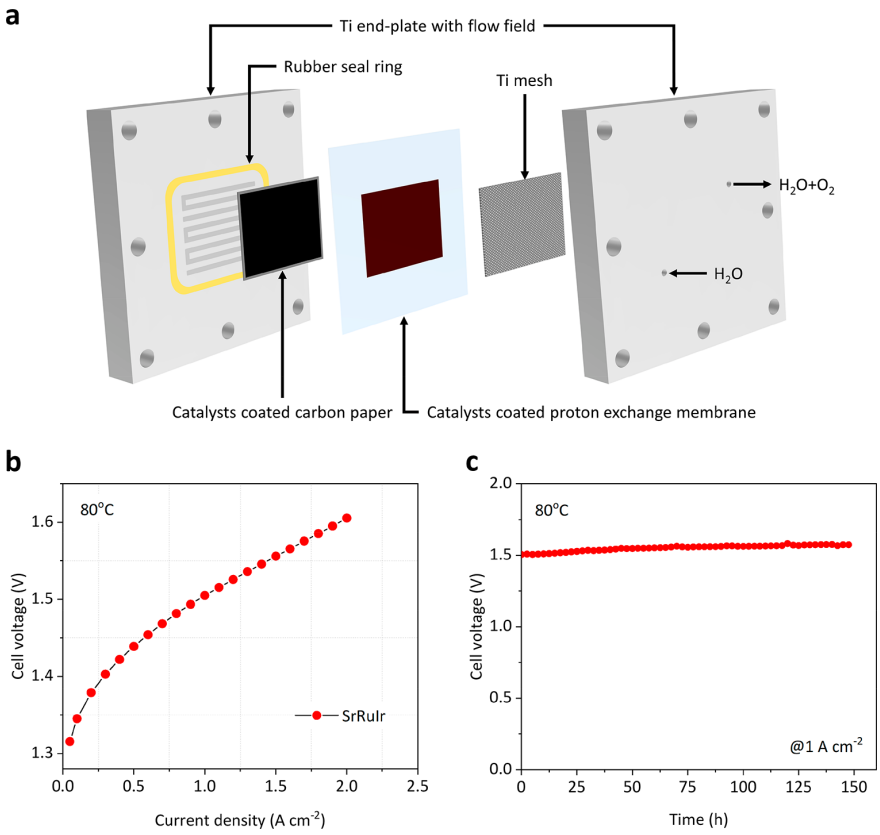

Figure 5. PEM electrolyzer demonstration. (a) Schematic diagram of the PEM electrolyzer. (b) Steady-state polarization curve of a PEM electrolyzer measured at 80 °C using SrRuIr as anodic catalysts. (c) Chronopotentiometry tests of the SrRuIr oxide catalyst at 1 A cm^{-2} in the PEM electrolyzer measured at 80 °C.

was observed in the SrRu sample (Figure S29), while the valence of Ru in RuO_2 and RuIr controls remained at +4 (Figure S30 and S31). Bader charge analysis from DFT calculations similarly showed that Ru is more positively charged than RuO_2 after Sr incorporation (Table S13). The Ru 3p XPS data suggested possible formation of high-valence Ru species on the surface (Figure S32). The above results support that Sr modulation has a role in the promotion of high-valence Ru sites, which are known to be more active than Ru^{4+} species.[35,36]

Furthermore, SrRuIr samples had a significantly higher white-line intensity than pristine RuO_2 without peak splitting at ~2840 eV (Figure 4b), showing that more unoccupied states were generated in the e_g states of Ru after Sr incorporation.[37,38] This was further proven by partial density of states (PDOS) analysis of surface Ru sites from DFT calculations (Figure 4c). We suggest that the incorporation of Sr modulated the electronic structure of Ru by contributing the unoccupied e_g state to the Ru active sites at *ca.* 1 eV above Fermi level (Figure S33). Since the e_g orbitals directly participate in the σ-bonding with surface adsorbates,[39,40] the e_g occupancy can affect the binding of oxo-intermediates in the AEM, thus facilitating OER. Though a portion of Sr may leach during OER, the remaining Sr appears to affect the electronic structure of Ru (Supplementary Note 3 of the Supporting Information). The Ir L_3-edge white line position of SrRuIr and RuIr were shifted in the positive direction compared to IrO_2, confirming the interaction between Ru−O−Ir (Figure 4d). The valence change of Ir is also supported by XPS (Figure S34). Sr incorporation leads to a more positive and higher white line peak than in RuIr, indicating the formation of more *d*-band holes of Ir and the increased covalency of the Ir−O bond, contributors toward high activity in OER.[41]

Water Electrolysis Demonstration in PEM. To further evaluate the performance of SrRuIr in industrial operating systems, we next used the catalyst in a PEM electrolyzer at 80 °C (Figure 5a and Figure S35). The steady-state polarization curves in Figure 5b indicate that the OER activity of SrRuIr reduced the overall cell voltage to 1.50 V at 1 A cm^{-2}, which is superior to the prior best report (Table S14). Upon applying a constant current of 1 A cm^{-2}, no significant increase in cell voltage was observed after 150 h of electrolysis (Figure 5c).

CONCLUSIONS

In this work, we predicted the OER activity and stability of a Sr−Ru−Ir ternary system by DFT and then successfully synthesized a SrRuIr oxide electrocatalyst. The catalysts exhibited an overpotential of only 223 mV after 1,500 h at 10 mA cm^{-2}. The EXAFS and DEMS measurements showed that the high stability originated from a strong interaction among Ru−O−Ir local structures and a suppressed LOM pathway, preventing the dissolution of the catalyst. Our in situ XAS and DFT calculations indicated that the binding energetics of oxo-intermediates on high-valence Ru sites

https://doi.org/10.1021/jacs.1c00384
J. Am. Chem. Soc. 2021, 143, 6482−6490

were optimized by Sr and Ir incorporation. This work will inform the development of highly active and stable electrocatalysts for OER, as well as other electrocatalysis applications.

■ ASSOCIATED CONTENT

Supporting Information

The Supporting Information is available free of charge at https://pubs.acs.org/doi/10.1021/jacs.1c00384.

Methods and figures, turnover frequency (TOF) calculations (Supplementary Note 1), XAS measurements and analysis (Supplementary Note 2), leaching of Sr (Supplementary Note 3), and effect of solvent in DFT calculations (Supplementary Note 4) (PDF)

■ AUTHOR INFORMATION

Corresponding Authors

Bo Zhang − *State Key Laboratory of Molecular Engineering of Polymers, Department of Macromolecular Science and Laboratory of Advanced Materials, Fudan University, Shanghai 200438, China;* orcid.org/0000-0002-7853-979X; Email: bozhang@fudan.edu.cn

Huisheng Peng − *State Key Laboratory of Molecular Engineering of Polymers, Department of Macromolecular Science and Laboratory of Advanced Materials, Fudan University, Shanghai 200438, China;* orcid.org/0000-0003-3746-8494; Email: penghs@fudan.edu.cn

Edward H. Sargent − *Department of Electrical and Computer Engineering, University of Toronto, Toronto, Ontario M5S 3G4, Canada;* orcid.org/0000-0003-0396-6495; Email: ted.sargent@utoronto.ca

Authors

Yunzhou Wen − *State Key Laboratory of Molecular Engineering of Polymers, Department of Macromolecular Science and Laboratory of Advanced Materials, Fudan University, Shanghai 200438, China*

Peining Chen − *State Key Laboratory of Molecular Engineering of Polymers, Department of Macromolecular Science and Laboratory of Advanced Materials, Fudan University, Shanghai 200438, China; Department of Electrical and Computer Engineering, University of Toronto, Toronto, Ontario M5S 3G4, Canada*

Lu Wang − *Institute of Functional Nano & Soft Materials (FUNSOM) and Jiangsu Key Laboratory for Carbon-Based Functional Materials & Devices, Soochow University, Suzhou 215123, China; Materials and Process Simulation Center (MSC) and Joint Center for Artificial Photosynthesis (JCAP), California Institute of Technology, Pasadena, California 91125, United States;* orcid.org/0000-0003-0552-1385

Shangyu Li − *State Key Laboratory of Molecular Engineering of Polymers, Department of Macromolecular Science and Laboratory of Advanced Materials, Fudan University, Shanghai 200438, China*

Ziyun Wang − *Department of Electrical and Computer Engineering, University of Toronto, Toronto, Ontario M5S 3G4, Canada;* orcid.org/0000-0002-2817-8367

Jehad Abed − *Department of Electrical and Computer Engineering, University of Toronto, Toronto, Ontario M5S 3G4, Canada; Department of Materials Science & Engineering, University of Toronto, Toronto, Ontario M5S 1A1, Canada*

Xinnan Mao − *Institute of Functional Nano & Soft Materials (FUNSOM) and Jiangsu Key Laboratory for Carbon-Based Functional Materials & Devices, Soochow University, Suzhou 215123, China*

Yimeng Min − *Department of Electrical and Computer Engineering, University of Toronto, Toronto, Ontario M5S 3G4, Canada*

Cao Thang Dinh − *Department of Chemical Engineering, Queen's University, Kingston, Ontario K7L 3N6, Canada;* orcid.org/0000-0001-9641-9815

Phil De Luna − *Department of Electrical and Computer Engineering, University of Toronto, Toronto, Ontario M5S 3G4, Canada;* orcid.org/0000-0002-7729-8816

Rui Huang − *State Key Laboratory of Molecular Engineering of Polymers, Department of Macromolecular Science and Laboratory of Advanced Materials, Fudan University, Shanghai 200438, China*

Longsheng Zhang − *State Key Laboratory of Molecular Engineering of Polymers, Department of Macromolecular Science and Laboratory of Advanced Materials, Fudan University, Shanghai 200438, China*

Lie Wang − *State Key Laboratory of Molecular Engineering of Polymers, Department of Macromolecular Science and Laboratory of Advanced Materials, Fudan University, Shanghai 200438, China*

Liping Wang − *State Key Laboratory of Molecular Engineering of Polymers, Department of Macromolecular Science and Laboratory of Advanced Materials, Fudan University, Shanghai 200438, China*

Robert J. Nielsen − *Materials and Process Simulation Center (MSC) and Joint Center for Artificial Photosynthesis (JCAP), California Institute of Technology, Pasadena, California 91125, United States;* orcid.org/0000-0002-7962-0186

Huihui Li − *Department of Electrical and Computer Engineering, University of Toronto, Toronto, Ontario M5S 3G4, Canada*

Taotao Zhuang − *Department of Electrical and Computer Engineering, University of Toronto, Toronto, Ontario M5S 3G4, Canada*

Changchun Ke − *Institute of Fuel Cell, Shanghai Jiao Tong University, Shanghai 200240, China*

Oleksandr Voznyy − *Department of Electrical and Computer Engineering, University of Toronto, Toronto, Ontario M5S 3G4, Canada;* orcid.org/0000-0002-8656-5074

Yongfeng Hu − *Canadian Light Source Inc., Saskatoon SK S7N 2 V3, Saskatchewan, Canada*

Youyong Li − *Institute of Functional Nano & Soft Materials (FUNSOM) and Jiangsu Key Laboratory for Carbon-Based Functional Materials & Devices, Soochow University, Suzhou 215123, China;* orcid.org/0000-0002-5248-2756

William A. Goddard III − *Materials and Process Simulation Center (MSC) and Joint Center for Artificial Photosynthesis (JCAP), California Institute of Technology, Pasadena, California 91125, United States;* orcid.org/0000-0003-0097-5716

Complete contact information is available at: https://pubs.acs.org/10.1021/jacs.1c00384

Author Contributions

○Y.W., P.C., L.W., and S.L. contributed equally to this work.

Notes

The authors declare no competing financial interest.

https://doi.org/10.1021/jacs.1c00384
J. Am. Chem. Soc. 2021, 143, 6482−6490

■ ACKNOWLEDGMENTS

This work was supported by MOST (2016YFA0203302), NSFC (21634003, 51573027, 21875042, 21805044, and 21771170), STCSM (16JC1400702, 18QA140080, and 19QA140080), SHMEC (2017-01-07-00-07-E00062), and Yanchang Petroleum Group. This work was also supported by the Program for Eastern Scholars at Shanghai Institutions. This work was supported by the Ontario Research Fund - Research Excellence Program, NSERC, and the CIFAR Bio-Inspired Solar Energy program. The ex situ XAFS was carried out at the BL14W1 beamline, Shanghai Synchrotron Radiation Facility (SSRF). The in situ Ru K-edge and Ir L_3-edge XAFS was measured at the 1W1B beamline, Beijing Synchrotron Radiation Facility (BSRF). The in situ Ru L_3-edge measurements were carried out at the soft X-ray microcharacterization beamline (SXRMB) in Canadian Light Source (CLS). The STEM imaging part of this research was completed at the Analytical and Testing Center, Northwestern Polytechnical University. The Caltech studies were supported by the Joint Center for Artificial Photosynthesis, a DOE Energy Innovation Hub, supported through the Office of Science of the U.S. Department of Energy under Award DE-SC0004993, by NSF (CBET-1805022), and by DOE AMO.

■ REFERENCES

(1) Carmo, M.; Fritz, D. L.; Mergel, J.; Stolten, D. A comprehensive review on PEM water electrolysis. *Int. J. Hydrogen Energy* **2013**, *38* (12), 4901−4934.

(2) Spöri, C.; Kwan, J. T. H.; Bonakdarpour, A.; Wilkinson, D. P.; Strasser, P. The stability challenges of oxygen evolving catalysts: towards a common fundamental understanding and mitigation of catalyst degradation. *Angew. Chem., Int. Ed.* **2017**, *56* (22), 5994−6021.

(3) Seitz, L. C.; Dickens, C. F.; Nishio, K.; Hikita, Y.; Montoya, J.; Doyle, A.; Kirk, C.; Vojvodic, A.; Hwang, H. Y.; Norskov, J. K.; Jaramillo, T. F. A highly active and stable $IrO_x/SrIrO_3$ catalyst for the oxygen evolution reaction. *Science* **2016**, *353* (6303), 1011−1014.

(4) Reier, T.; Nong, H. N.; Teschner, D.; Schlogl, R.; Strasser, P. Electrocatalytic oxygen evolution reaction in acidic environments - reaction mechanisms and catalysts. *Adv. Energy Mater.* **2017**, *7* (1), 1601275.

(5) Cherevko, S.; Zeradjanin, A. R.; Topalov, A. A.; Kulyk, N.; Katsounaros, I.; Mayrhofer, K. J. J. Dissolution of noble metals during oxygen evolution in acidic media. *ChemCatChem* **2014**, *6* (8), 2219−2223.

(6) Rossmeisl, J.; Qu, Z. W.; Zhu, H.; Kroes, G. J.; Nørskov, J. K. Electrolysis of water on oxide surfaces. *J. Electroanal. Chem.* **2007**, *607* (1−2), 83−89.

(7) Hong, W. T.; Risch, M.; Stoerzinger, K. A.; Grimaud, A.; Suntivich, J.; Shao-Horn, Y. Toward the rational design of non-precious transition metal oxides for oxygen electrocatalysis. *Energy Environ. Sci.* **2015**, *8* (5), 1404−1427.

(8) Zagalskaya, A.; Alexandrov, V. Role of defects in the interplay between adsorbate evolving and lattice oxygen mechanisms of the oxygen evolution reaction in RuO_2 and IrO_2. *ACS Catal.* **2020**, *10* (6), 3650−3657.

(9) Geiger, S.; Kasian, O.; Ledendecker, M.; Pizzutilo, E.; Mingers, A. M.; Fu, W. T.; Diaz-Morales, O.; Li, Z.; Oellers, T.; Fruchter, L.; Ludwig, A.; Mayrhofer, K. J. J.; Koper, M. T. M.; Cherevko, S. The stability number as a metric for electrocatalyst stability benchmarking. *Nat. Catal.* **2018**, *1* (7), 508−515.

(10) Grimaud, A.; Demortière, A.; Saubanère, M.; Dachraoui, W.; Duchamp, M.; Doublet, M.-L.; Tarascon, J.-M. Activation of surface oxygen sites on an iridium-based model catalyst for the oxygen evolution reaction. *Nat. Energy* **2017**, *2* (1), 16189.

(11) Grimaud, A.; Diaz-Morales, O.; Han, B.; Hong, W. T.; Lee, Y. L.; Giordano, L.; Stoerzinger, K. A.; Koper, M. T. M.; Shao-Horn, Y. Activating lattice oxygen redox reactions in metal oxides to catalyse oxygen evolution. *Nat. Chem.* **2017**, *9* (5), 457−465.

(12) Huang, Z.-F.; Song, J.; Du, Y.; Xi, S.; Dou, S.; Nsanzimana, J. M. V.; Wang, C.; Xu, Z. J.; Wang, X. Chemical and structural origin of lattice oxygen oxidation in Co-Zn oxyhydroxide oxygen evolution electrocatalysts. *Nat. Energy* **2019**, *4* (4), 329−338.

(13) Zhang, L.; Wang, L.; Wen, Y.; Ni, F.; Zhang, B.; Peng, H. Boosting Neutral Water Oxidation through Surface Oxygen Modulation. *Adv. Mater.* **2020**, *32* (31), No. 2002297.

(14) Yao, Y.; Hu, S.; Chen, W.; Huang, Z.-Q.; Wei, W.; Yao, T.; Liu, R.; Zang, K.; Wang, X.; Wu, G.; Yuan, W.; Yuan, T.; Zhu, B.; Liu, W.; Li, Z.; He, D.; Xue, Z.; Wang, Y.; Zheng, X.; Dong, J.; Chang, C.-R.; Chen, Y.; Hong, X.; Luo, J.; Wei, S.; Li, W.-X.; Strasser, P.; Wu, Y.; Li, Y. Engineering the electronic structure of single atom Ru sites via compressive strain boosts acidic water oxidation electrocatalysis. *Nat. Catal.* **2019**, *2* (4), 304−313.

(15) Chen, S.; Huang, H.; Jiang, P.; Yang, K.; Diao, J.; Gong, S.; Liu, S.; Huang, M.; Wang, H.; Chen, Q. Mn-doped RuO_2 nanocrystals as highly active electrocatalysts for enhanced oxygen evolution in acidic media. *ACS Catal.* **2020**, *10* (2), 1152−1160.

(16) Lin, Y.; Tian, Z.; Zhang, L.; Ma, J.; Jiang, Z.; Deibert, B. J.; Ge, R.; Chen, L. Chromium-ruthenium oxide solid solution electrocatalyst for highly efficient oxygen evolution reaction in acidic media. *Nat. Commun.* **2019**, *10* (1), 162.

(17) Su, J.; Ge, R.; Jiang, K.; Dong, Y.; Hao, F.; Tian, Z.; Chen, G.; Chen, L. Assembling ultrasmall copper-doped ruthenium oxide nanocrystals into hollow porous polyhedra: Highly robust electrocatalysts for oxygen evolution in acidic media. *Adv. Mater.* **2018**, *30*, 1801351, .

(18) Schweinar, K.; Gault, B.; Mouton, I.; Kasian, O. Lattice oxygen exchange in rutile IrO_2 during the oxygen evolution reaction. *J. Phys. Chem. Lett.* **2020**, *11* (13), 5008−5014.

(19) Chen, Y.; Li, H.; Wang, J.; Du, Y.; Xi, S.; Sun, Y.; Sherburne, M.; Ager, J. W., 3rd; Fisher, A. C.; Xu, Z. J. Exceptionally active iridium evolved from a pseudo-cubic perovskite for oxygen evolution in acid. *Nat. Commun.* **2019**, *10* (1), 572.

(20) Kim, J.; Shih, P. C.; Tsao, K. C.; Pan, Y. T.; Yin, X.; Sun, C. J.; Yang, H. High-performance pyrochlore-type yttrium ruthenate electrocatalyst for oxygen evolution reaction in acidic media. *J. Am. Chem. Soc.* **2017**, *139* (34), 12076−12083.

(21) Kuznetsov, D. A.; Naeem, M. A.; Kumar, P. V.; Abdala, P. M.; Fedorov, A.; Muller, C. R. Tailoring lattice oxygen binding in Ruthenium pyrochlores to enhance oxygen evolution activity. *J. Am. Chem. Soc.* **2020**, *142* (17), 7883−7888.

(22) Stoerzinger, K. A.; Rao, R. R.; Wang, X. R.; Hong, W. T.; Rouleau, C. M.; Shao-Horn, Y. The role of Ru redox in pH-dependent oxygen evolution on rutile ruthenium dioxide surfaces. *Chem.* **2017**, *2* (5), 668−675.

(23) Kötz, R.; Stucki, S. Stabilization of RuO_2 by IrO_2 for anodic oxygen evolution in acid media. *Electrochim. Acta* **1986**, *31* (10), 1311−1316.

(24) Cheng, J.; Zhang, H.; Chen, G.; Zhang, Y. Study of $IrxRu_{1-x}O_2$ oxides as anodic electrocatalysts for solid polymer electrolyte water electrolysis. *Electrochim. Acta* **2009**, *54* (26), 6250−6256.

(25) Danilovic, N.; Subbaraman, R.; Chang, K. C.; Chang, S. H.; Kang, Y.; Snyder, J.; Paulikas, A. P.; Strmcnik, D.; Kim, Y. T.; Myers, D.; Stamenkovic, V. R.; Markovic, N. M. Using surface segregation to design stable Ru-Ir oxides for the oxygen evolution reaction in acidic environments. *Angew. Chem., Int. Ed.* **2014**, *53* (51), 14016−14021.

(26) Escudero-Escribano, M.; Pedersen, A. F.; Paoli, E. A.; Frydendal, R.; Friebel, D.; Malacrida, P.; Rossmeisl, J.; Stephens, I. E. L.; Chorkendorff, I. Importance of surface IrO_x in stabilizing RuO_2 for oxygen evolution. *J. Phys. Chem. B* **2018**, *122* (2), 947−955.

(27) Stoerzinger, K. A.; Qiao, L.; Biegalski, M. D.; Shao-Horn, Y. Orientation-dependent oxygen evolution activities of rutile IrO_2 and RuO_2. *J. Phys. Chem. Lett.* **2014**, *5* (10), 1636−1641.

https://doi.org/10.1021/jacs.1c00384
J. Am. Chem. Soc. 2021, 143, 6482−6490

(28) Zhang, B.; Zheng, X.; Voznyy, O.; Comin, R.; Bajdich, M.; Garcia-Melchor, M.; Han, L.; Xu, J.; Liu, M.; Zheng, L.; Garcia de Arquer, F. P.; Dinh, C. T.; Fan, F.; Yuan, M.; Yassitepe, E.; Chen, N.; Regier, T.; Liu, P.; Li, Y.; De Luna, P.; Janmohamed, A.; Xin, H. L.; Yang, H.; Vojvodic, A.; Sargent, E. H. Homogeneously dispersed multimetal oxygen-evolving catalysts. *Science* **2016**, *352* (6283), 333−337.
(29) Miao, X.; Zhang, L.; Wu, L.; Hu, Z.; Shi, L.; Zhou, S. Quadruple perovskite ruthenate as a highly efficient catalyst for acidic water oxidation. *Nat. Commun.* **2019**, *10* (1), 3809.
(30) Hodnik, N.; Jovanovič, P.; Pavlišič, A.; Jozinović, B.; Zorko, M.; Bele, M.; Šelih, V. S.; Šala, M.; Hočevar, S.; Gaberšček, M. New insights into corrosion of ruthenium and ruthenium oxide nanoparticles in acidic media. *J. Phys. Chem. C* **2015**, *119* (18), 10140−10147.
(31) Xia, Z.; Zhang, H.; Shen, K.; Qu, Y.; Jiang, Z. Wavelet analysis of extended X-ray absorption fine structure data: Theory, application. *Phys. B* **2018**, *542*, 12−19.
(32) Huang, Y. S.; Pollak, F. H. Raman investigation of rutile RuO_2. *Solid State Commun.* **1982**, *43* (12), 921−924.
(33) Pavlovic, Z.; Ranjan, C.; Gao, Q.; van Gastel, M.; Schlögl, R. Probing the structure of a water-oxidizing anodic iridium oxide catalyst using Raman spectroscopy. *ACS Catal.* **2016**, *6* (12), 8098−8105.
(34) Choy, J.-H.; Kim, J.-Y.; Hwang, S.-H.; Kim, S.-J.; Demazeau, G. Soft XAFS study on the 4d electronic structure of ruthenium in complex perovskite oxide. *Int. J. Inorg. Mater.* **2000**, *2* (1), 61−70.
(35) Feng, Q.; Wang, Q.; Zhang, Z.; Xiong, Y. Y. H.; Li, H. Y.; Yao, Y.; Yuan, X. Z.; Williams, M. C.; Gu, M.; Chen, H.; Li, H.; Wang, H. J. Highly active and stable ruthenate pyrochlore for enhanced oxygen evolution reaction in acidic medium electrolysis. *Appl. Catal., B* **2019**, *244*, 494−501.
(36) Chang, S. H.; Danilovic, N.; Chang, K. C.; Subbaraman, R.; Paulikas, A. P.; Fong, D. D.; Highland, M. J.; Baldo, P. M.; Stamenkovic, V. R.; Freeland, J. W.; Eastman, J. A.; Markovic, N. M. Functional links between stability and reactivity of strontium ruthenate single crystals during oxygen evolution. *Nat. Commun.* **2014**, *5*, 4191.
(37) Kim, J. Y.; Hwang, S. H.; Kim, S. J.; Demazeau, G.; Choy, J. H.; Shimada, H. 4d electronic structure analysis of ruthenium in the perovskite oxides by Ru K- and L-edge XAS. *J. Synchrotron Radiat.* **2001**, *8* (2), 722−724.
(38) Choy, J.-H.; Kim, D.-K.; Demazeau, G.; Jung, D.-Y. L_{III}-Edge XANES study on unusually high valent iridium in a perovskite lattice. *J. Phys. Chem.* **1994**, *98* (25), 6258−6262.
(39) Suntivich, J.; May, K. J.; Gasteiger, H. A.; Goodenough, J. B.; Shao-Horn, Y. A perovskite oxide optimized for oxygen evolution catalysis from molecular orbital principles. *Science* **2011**, *334* (6061), 1383−1385.
(40) Betley, T. A.; Wu, Q.; Van Voorhis, T.; Nocera, D. G. Electronic design criteria for O-O bond formation via metal-oxo complexes. *Inorg. Chem.* **2008**, *47* (6), 1849−1861.
(41) Nong, H. N.; Reier, T.; Oh, H.-S.; Gliech, M.; Paciok, P.; Vu, T. H. T.; Teschner, D.; Heggen, M.; Petkov, V.; Schlögl, R.; Jones, T.; Strasser, P. A unique oxygen ligand environment facilitates water oxidation in hole-doped $IrNiO_x$ core-shell electrocatalysts. *Nat. Catal.* **2018**, *1* (11), 841−851.

https://doi.org/10.1021/jacs.1c00384
J. Am. Chem. Soc. 2021, 143, 6482−6490